Composition-driven transition from amorphous to crystalline films enables bottom-up design of functional surfaces

A. Borroto, A.C. C García-Wong, S. Bruyère, S. Migot, D. Pilloud, J.F. F Pierson, F. Mücklich, David Horwat

Composition-driven transition from amorphous to crystalline films enables bottom-up design of functional surfaces

A. Borroto [a,b], A.C. García-Wong [a], S. Bruyère [a], S. Migot [a], D. Pilloud [a], J.F. Pierson [a], F. Mücklich [b] and D. Horwat [a,*]

[a] Université de Lorraine, CNRS, IJL, F-54000 Nancy, France.

[b] Department of Materials Science and Engineering, Chair of Functional Materials, Saarland University, Campus D3.3, D-66123 Saarbrücken, Germany.

*david.horwat@univ-lorraine.fr

Abstract

Composition-driven transition to the crystalline state is characteristic of amorphous metal alloys and is widely observed in thin film. However, the transition zone (compositional range between single-phase amorphous and crystalline films) remains unexplored. Here, we demonstrate that this transition offers an excellent scenario for the fabrication of hybrid crystalline-amorphous architectures. The peculiar morphology of these nano(micro)-structured films provides a simple bottom-up route, applicable to a broad range of alloys, for obtaining adjustable multifunctional surfaces. In particular, we prove the feasibility of this approach as a one-step process for a precise control of specular and diffuse reflectance over the visible spectrum. Further, the growth kinetics of the formed two-phase nanostructures is demonstrated equivalent to a 2-dimensional amorphous-to-crystalline phase transformation. Using Zr-W alloys as a model system, fundamental parameters of the growth process and the corresponding metastable thickness-composition phase diagram are extracted. It evidences

that the two-phase nanostructures, despite occurring in a wide range of compositions, can be easily hidden experimentally by growth kinetics and nucleation delay. These results open a new avenue on the surface morphology and related functional properties control in thin films.

Keywords: Thin films, Amorphous metal alloys, Nanocrystalline alloys, Phase separation, Growth kinetics, Surface functionalization.

1. Introduction

Along the ages, biological species have developed specific geometrical features at their skin, shell, hairs, or more generally at their interfaces with the environment. Those are associated to specific capabilities, such as self-cleaning [1], improved adhesion [2], anti-reflection [3], iridescence [4], drag reduction [5], to cite a few. Nature inspires us to develop materials and objects with new functionalities, acting on their surface topography at different scales being one of the main levers at hand. Top-down approaches have naturally emerged as they enable to mimic the surface topography of biological species, and benefit from their long-term evolution, in order to modulate functional properties to a large extent [6–12]. Yet, it is often at the expense of costly and/or complex structuration processes. This is calling for new methods in which the topography develops during material synthesis, i.e. in a bottom-up way, and still offers a sensitive control over the functional properties.

Among the many approaches to modify surface properties, thin film deposition has established itself as an important way of materials functionalization with low raw materials consumption, which is highly sought in the current world. Most reported studies rely on the inherent properties of the deposited materials or modification of their microstructure to adjust surface properties [13–15]. In this context, physical vapor deposition methods are particularly attractive as they are suited to grow thin layers of almost any material on any other one, e.g. metal on polymer, ceramics on metal or wood, and to bring the surface properties of the deposit to a specific object under very few restrictions. Structure zone models have established important guidelines to understand how the morphology of a single-phased film can be manipulated through experimental and physical parameters and have paved the way of thin film science over the last 50 years [16–18]. Additionally, since the condensation process from the vapor phase to form a solid film occurs in a very short time, it is associated to very high quenching rates (~10^6-10^9 K s^{-1}). Hence, the film structure, microstructure and bonding

state can be manipulated to a very large extent between far-out and close-to-stable thermodynamic equilibrium conditions, depending on deposition conditions. Thin film amorphous metal alloys are an extreme example of such possibilities, in which nucleation is inhibited [19–25]. In less drastic conditions, when crystal growth is limited but nucleation occurs, nanocrystalline films can be obtained. A wide range of unusual properties arise from such configurations, like ultra-high plasticity [26], antibacterial activity [27,28], and high corrosion and wear resistance [29–31]. Yet, in most cases, single-phased coatings are considered and the mechanisms at the origin of multi-phased coatings and their potentialities remain essentially unexplored. In particular, the composition-driven transition between amorphous metal alloys and nanocrystalline films [32], at the core of the present study, has been overlooked so far as a possible way of surface functionalization and little is known about the nature of such transition, despite it occurs in many systems [31,33–37].

Here, we show that composition-driven transition from amorphous to crystalline state in thin films proceeds by competitive growth between the two states and is associated to gradual, yet intense, change in the surface topography. Within this transition, crystalline regions terminated by domes, nucleate inside, overgrow and protrude from, amorphous flat thin film matrix. Surface morphology-related functional properties are hence controlled, such as wettability or components of the optical reflectance. To serve as a platform for future developments and explorations, we also establish a kinetic model and phase diagram of the process. These are based on the modular kinetics model (MKM) [38–41] and the equivalence between the observed topographic evolution at the film surface and a 2-dimensional (2D) phase transformation.

2. Experimental details

Thin films synthesis: Nanostructured Zr-W and Zr-Mo thin films were deposited on (100) silicon single crystal substrates (1.5 x 1.5 cm^2) using DC magnetron co-sputtering of Zr and W

or Mo metallic targets in the presence of argon. To ensure homogeneity of the films, all the depositions were made with the targets in confocal configuration and the substrate holder in rotating mode (Figure 1a). The sputtering chamber was pumped down via a mechanical and a turbo-molecular pumps allowing a base vacuum of 10^{-6} Pa. The targets to substrate distance was fixed at 9 cm and working argon pressures of 2 and 3 Pa were used for the Zr-Mo and Zr-W films, respectively. The chemical composition of the films was controlled by applying a discharge current of 0.3 A to the Zr target and 0.4, 0.5 and 0.55 A to the W target or 0.28 A to the Mo target (targets dimension: 50.8 mm in diameter, 3 mm-thick and purity higher than 99.9%, both were powered by an Maxim 1000 DC generator). Under these conditions, Zr-W films with W content of 67, 72 and 74 at% and Zr-Mo films with 60 at% of Mo content were obtained. The films were deposited without external heating. The self-established temperature at the substrate was measured using a thermocouple and did not exceed 55 °C during growth.

Thin films characterization: X-ray diffraction measurements were conducted in the Bragg-Brentano configuration with $K_{\alpha}Cu$ radiation (λ=1.5406 Å) using an AXS Bruker D8 Advance diffractometer. To analyze the surface morphology of the samples, scanning electron micrographs were taken in a Philips XL-30 S-FEG scanning electron microscope. TEM investigations were performed using a cold FEG JEOL ARM200 microscope. For this analysis, cross-section TEM samples of films were prepared using a focused ion beam (FIB)-scanning electron microscope dual beam system (FEI Helios 600). Throughout the FIB process, the time during the ionic cuts was the shortest possible to avoid any heating effect.

Reflectance measurements: The reflectance was measured in the 350-900 nm range using a Varian Cary 5000 UV-vis-NIR spectrophotometer with an integrating sphere coupled.

Contact angle measurements: Contact angle measurements of water droplets of 1.14 µL were carried out under ambient conditions (25 °C) using a GBX DIGIDROP Contact Angle Meter. Measurements were performed five seconds after droplet deposition. For each sample, several

different droplets were deposited on the film surface and the average contact angle was determined.

3. Results and discussion

3.1. Control of the surface-related properties through nanocrystalline-amorphous competitive growth

Given the properties of metals, metallic coatings are attractive to provide to objects a wide variety of functions such as metallic shine, scratch resistance, resistance to permeation and electrical conductivity. Zr-based metallic alloy films are prone to amorphization for some compositions and hold exceptional properties like very high hardness, ultralow friction, and high corrosion resistance in acidic media [31,42]. Here, we resort on the Zr-W and Zr-Mo as model systems that exhibit composition-driven structural change from amorphous to crystalline, to extend the control over functional properties and study related film growth kinetics. Owing to the ability of the condensation process to produce far-out-of-equilibrium states, co-sputtering zirconium with molybdenum or tungsten (Figure 1a), a composition-driven transition from X-ray amorphous to crystalline Mo(Zr) and W(Zr) supersaturated solid solutions are obtained (Figure 1b). This markedly contrasts with the Zr-Mo and Zr-W equilibrium phase diagrams in which only stable primary crystalline solid solutions and the C15 $ZrMo_2$ and ZrW_2 Laves phases exist and show very low solubilities [43,44]. Similar observations were made in many chemical systems [45,46]. Interestingly, within the transition zone, X-ray diffraction evidences the above-mentioned amorphous and crystalline phases can exist together (Figure 1b; Figure S1 and Figure S2, Supporting Information).

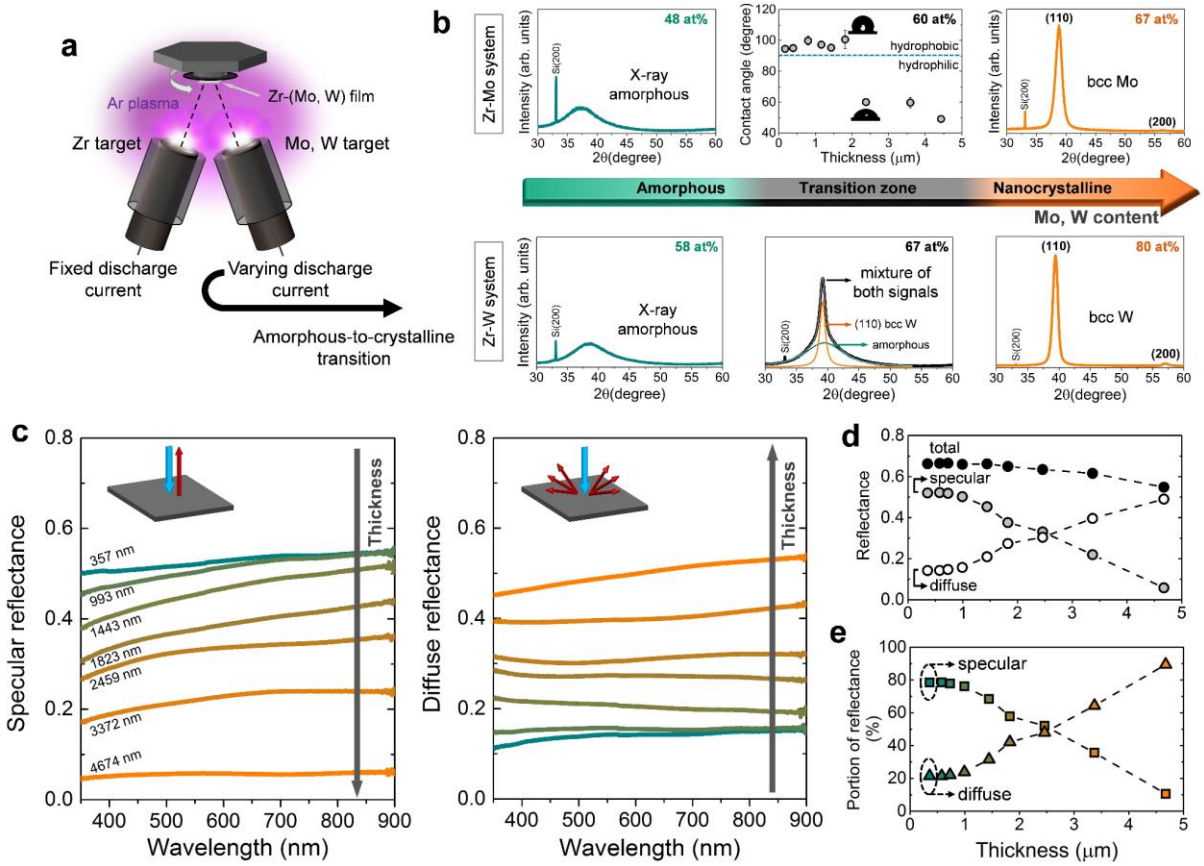

Figure 1. Composition-driven amorphous-to-crystalline transition in thin films allows controlling the surface-related properties. (a) Schematic of the sputtering chamber used for depositing binary metallic alloys. By changing the electrical parameters of the cathodes, the chemical composition of the alloys can be controlled. (b) X-ray diffractograms of films with 48 at% Mo or 58 at% W (left) and 67 at% Mo or 80 at% W (right) showing that a composition-driven transition from an amorphous to a crystalline structure occurs in the Zr-Mo and Zr-W systems. In the transition zone (center), the wettability of 60 at% Mo films can be thickness-switched from hydrophobic to hydrophilic. X-ray diffractogram of 67 at% W film is composed by the overlapped signals from amorphous and crystalline phases. (c) Evolution of specular (left) and diffuse (right) reflectance spectra at normal incidence with the increases of thickness of 67 at% W films. (d) Evolution with thickness of the total reflectance and its specular and diffuse components at a wavelength of 550 nm of 67 at% W films. (e) Evolution with thickness of the proportions of specular and diffuse reflectance components with respect to the total reflectance at the same wavelength and film composition.

Varying the film thickness in this zone, surface-related functional properties can be tuned to a large extent. It is first highlighted (Figure 1b) in change of the surface wettability for Zr-Mo films that turn from hydrophobic to hydrophilic at large deposition thickness. This indicates the film microstructure likely evolve during growth, as will be confirmed later. A common interpretation of such behavior is the percolation of hydrophobic regions of the surface [47]. We do not elaborate further on this effect (see Supplementary Note, Supporting Information for details on the relation between surface morphology and contact angle). Yet, we expect it to be useful to structure the wettability of a surface, without the need of post synthesis texturing or chemical functionalization, by simply masking some regions between two sequences of deposition process. In Zr-W films whose composition lies within the transition zone, it is found that the specular and diffuse components of the reflectance exhibit opposite trends with the film thickness (Figure 1c-e; Figure S3, Supporting Information): diffuse (specular) reflectance strongly increases (decreases) while the total reflectance decreases by only approx. 14% with thickness. This simple strategy to manipulate reflectance components based on the film thickness as a control parameter contrasts with the previously reported possibility of manipulation through the size of metal nanoparticles in polymer/metal hybrid systems [48]. The spectral response (Figure 1c) evidences that reflectance components can be controlled over the entire visible region. Moreover, it is noticeable that conditions can be found for which nearly constant reflectivity is obtained. A practical consequence is the possibility to reflect an optical object or signal homogeneously over all visible wavelengths, i.e. without color changes. The proportions of specular and diffuse components can be selected almost freely (Figure 1d,e). Overall, this is a new possibility to modify in a simple way the appearance of an object from bright to matt metallic, to manipulate and shape visible light. Opportunities of applications cover, among others, the fields of decoration, photography, reflective cavities in LEDs and solar energy harvesting. By changing the composition within

the transition zone, the phenomenon is still observed but at different change rates and amplitudes (more details in Figure S3, Supporting Information). In metals, diffuse reflectance is the result of the surface morphology. The possibility to manipulate the diffuse reflectance at different wavelengths is a clue for the intervention of a hierarchical structure in the process, which deserves further attention. In order to derive a comprehensive understanding on how the control over surface-related functional properties emerge through modifications of the surface morphology and with the aim to build a platform for future applications, the dynamics and microstructure of the amorphous-to-crystalline transition needs to be revealed.

Investigation of the film microstructure discloses that the underlying process in action in the transition zone is the competitive growth between the crystalline and amorphous phases, the crystalline phase progressively overgrowing the amorphous one (Figure 2). Figure 2a shows the evolution of top-view scanning electron microscopy (SEM) images as a function of film thickness for three different compositions (67, 72 and 74 at% W) within the transition zone in the Zr-W system. SEM observations evidence that the crystalline nuclei, whose density is controlled through the chemical composition, expend laterally as film grows. Cross-section transmission electron microscopy (TEM) analyses (Figure 2b-e) bring additional information: crystalline regions are of conical shape inside the amorphous matrix and are terminated by a dome whose base is aligned with the film surface. Moreover, they are constituted by bundles of nanoscale dendritic grains. The rise of diffuse reflectance and concomitant decay of specular reflectance is attributable to the progressive overgrowth of the amorphous phase by the crystalline phase regions acting as scattering sites. A similar process appears to be in action in other systems than binary metallic alloys, e.g. Al-N and Ti-O [49,50], but details about the dynamics and modelling are missing. Quantitative analysis and understanding of this process dynamics are needed in order to foster the dissemination of this new possibility of

control over the microstructure and properties. Therefore, the following section is dedicated to modelling the kinetics of this competitive growth process.

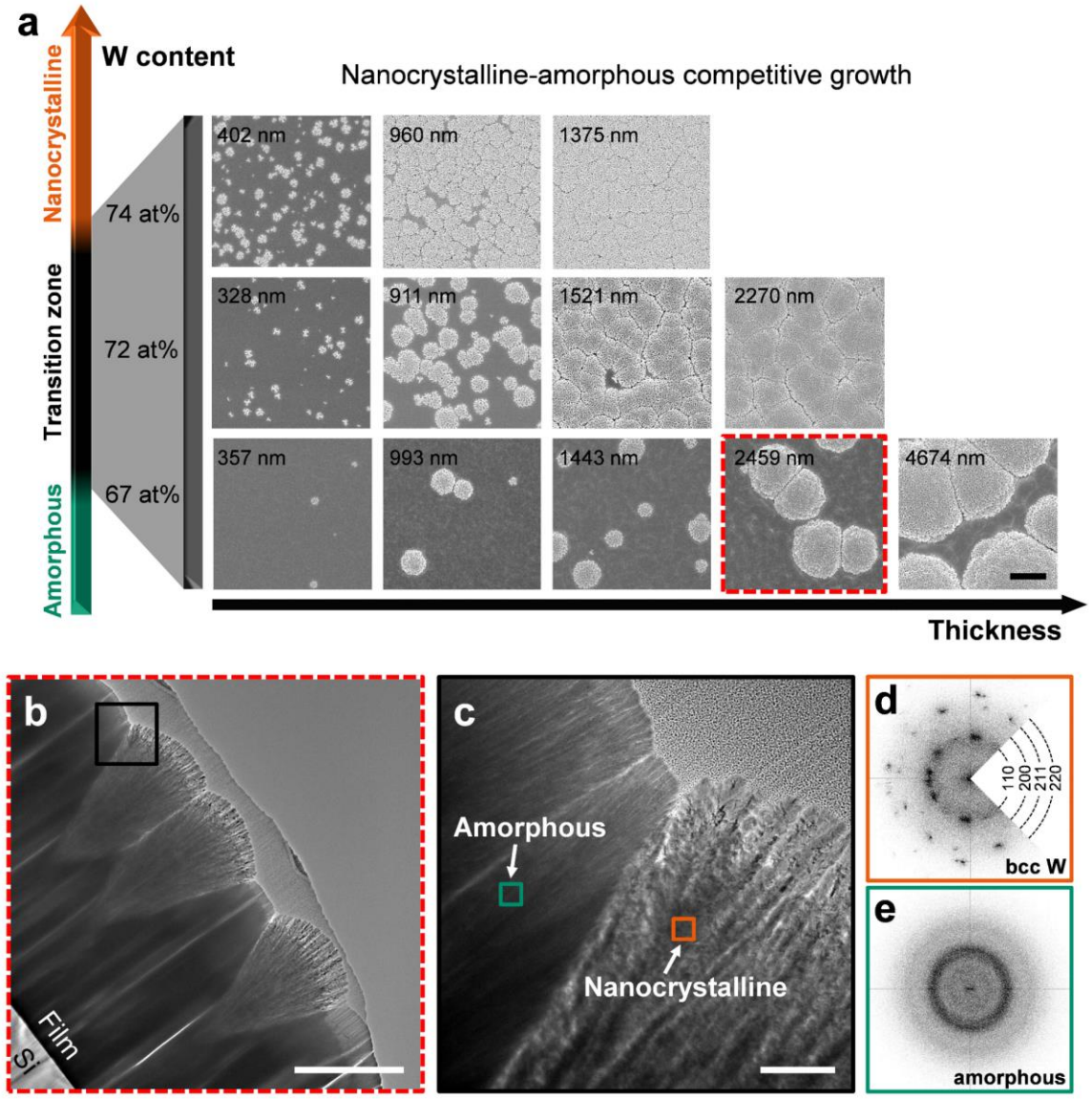

Figure 2. Nanocrystalline-amorphous competitive growth in sputter-deposited thin films. (a) Top-view SEM images showing the evolution of the surface morphology with composition and thickness of sputter-deposited Zr-W thin films synthesized in the transition zone. Scale bar: 1 µm. (b) Cross-sectional TEM image of sample highlighted in (a) evidencing the nanocrystalline-amorphous phase separation. Scale bar: 1 µm. (c) Zoom of image shown in (b). Scale bar: 100 nm. HRTEM images of regions highlighted with orange and green squares can be found in Figure S4, Supporting Information. (d) Fast Fourier transform (FFT) from the region highlighted with an orange square in (c). (e) FFT from the region highlighted with a green square in (c).

3.2. Kinetic model and thickness-composition phase diagram of the process

From the analysis of the top-view SEM images (Figure 2a), two magnitudes defining the kinetics of nanocrystalline-amorphous competitive growth can be tracked as a function of composition and thickness, i.e. the density of nanocrystalline nuclei N and the coverage of the film surface by the nanocrystalline phase S (see Supplementary Method, Supporting Information). Analytical expressions of both magnitudes can be deduced using the MKM approach for phase transformations [38–41]. This efficiently describes the process despite competitive growth is not a phase transformation: the nanocrystalline phase grows in competition with, but is not transforming from, the amorphous one. That is, the regions that condensate in an amorphous phase at a given film thickness keep their amorphous structure as the film continues growing. However, the surface morphology evolution with film thickness (Figure 3) is equivalent to an "apparent" 2D phase transformation, i.e. looking at the surface, the amorphous phase "seems" to be transforming into the nanocrystalline one. This equivalence allows using the formalism of 2D phase transformations to describe the kinetics of the 3D competitive growth between the amorphous and the nanocrystalline phases.

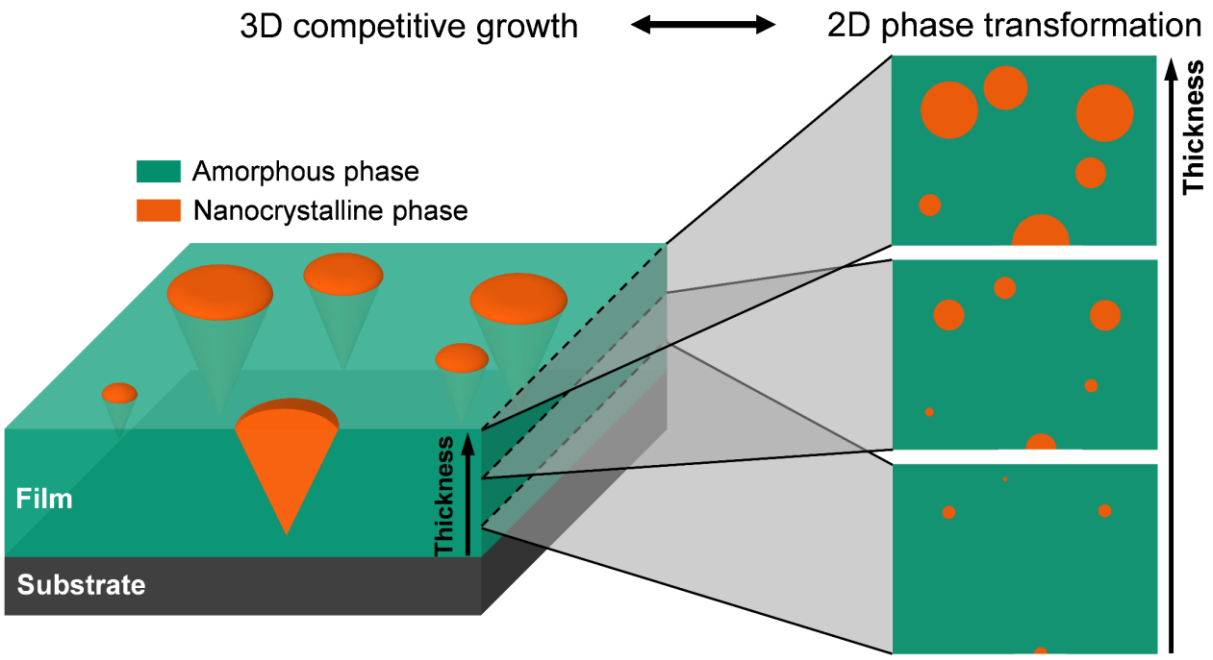

Figure 3. Equivalence between 3D nanocrystalline-amorphous competitive growth and 2D amorphous to crystalline phase transformation. Left panel: schematic of film presenting nanocrystalline-amorphous competitive growth. Right panel: top-view of the film at different thicknesses.

Supported by this equivalence, N and S can be written as a function of the film thickness h as (for deduction of Equation 1 and 2 see Appendix A, Equation A.5 and A.11 respectively)

$$N_{(h)} = N_0\left(1 - e^{-\gamma(h-h_c)}\right)\Theta[h - h_c] \quad (1)$$

and

$$S_{(h)} = 1 - \left(1 + (\xi - 1)\chi_{e_{(h)}}\right)^{-1/\xi - 1} \quad (2)$$

where N_0 is the total number of nanocrystalline nuclei per unit area when all of them are already nucleated, h_c is the critical thickness from which nucleation starts, γ is a parameter related with the nucleation rate (see Appendix A for more details). Θ is the unitary-step Heaviside function, reflecting the fact that there is a thickness, h_c, from which nucleation starts. In Equation 2, χ_e is the so-called extended transformed fraction, representing the

projected area, perpendicular to the growth direction of the film, of nanocrystalline regions if they could each nucleate and grow in the absence of other interfering growing nuclei. It can be expressed as a function of the same three free parameters than Equation 1, $\chi_e = f(N_0, h_c, \gamma)$ (Equation A.10, Appendix A). ξ is the so-called impingement parameter. When $\xi \to 1$, Equation 2 transforms into $S = 1 - e^{-\chi_e}$. It corresponds to the classical Kolmogorov-Johnson-Mehl-Avrami (KJMA) approach, in which a random nucleation of the nanocrystalline phase is assumed [51–55]. For $\xi > 1$, impingement of the nanocrystalline phase is stronger, indicating that nucleation occurs at specific sites, such as grain boundaries.

Figure 4a,b show the evolution with thickness of the density of nuclei and surface coverage by the nanocrystalline phase, together with the corresponding best fittings to the data. Obtained values for N_0, h_c and ξ are reported in Figure 4c,d. The increase in density of nanocrystalline nuclei and decrease of critical thickness for nucleation indicates more favorable conditions for nucleation when the W content increases. In the meantime, ξ evolves between values close to 2 and 1, corresponding to a transition from nucleation at specific sites when approaching to the composition of single-phase amorphous films towards random nucleation when approaching to the composition of single-phase nanocrystalline films. Microstructural analyzes indicate that nucleation is localized at the grain boundaries within the films for high ξ values (see Figure S5, Supporting Information). These findings shed the first light, in a quantitative way, on the nucleation process in the transition zone, indicating the main role played by grain boundaries.

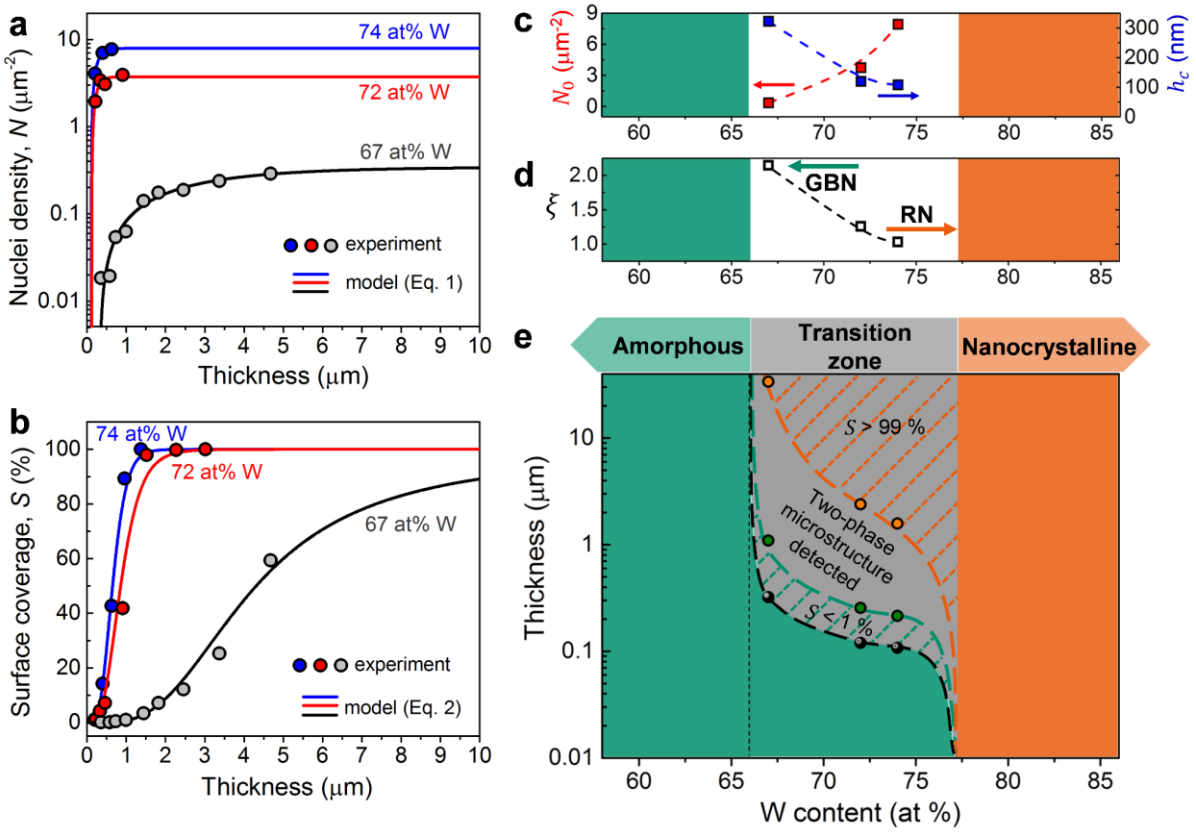

Figure 4. Thickness-composition metastable Zr-W phase diagram. (a) Evolution of the density of nanocrystalline nuclei and (b) surface coverage by the nanocrystalline phase with the increase of the film thickness for the three compositions studied. The dots represent the experimental data. In (a) the lines follow Equation 1. In (b) the lines follow Equation 2. (c) Values of N_0 (red squares) and h_c (blue squares) obtained from the fitting of Equation 1 to the data corresponding to the density of nanocrystalline nuclei. (d) Values of ξ obtained from the fitting of Equation 2 to the data corresponding to the surface coverage by the nanocrystalline phase. RN and GBN indicate random nucleation and grain boundaries nucleation, respectively. (e) Depending on composition, the structure of the films can be single-phased amorphous (green zone), single-phased nanocrystalline (orange zone) or bi-phased in the transition zone (gray zone). In this domain are shown the values of the critical thickness h_c (black points) and the thickness at which the surface coverage, S, is lower than 1% (green points) and higher than 99% (orange points). The last two thicknesses were calculated from extrapolation of Equation 2.

The proportion between the nanocrystalline and the amorphous phases in the transition zone can be controlled by varying either the composition or film thickness. The thickness-composition phase diagram of sputter-deposited Zr-W system can be determined around the transition zone by using the evolution of the density of nucleation sites N_0 with composition and considering the boundary conditions that it satisfies (see Appendix B). An important point in this diagram (Figure 4e) is the wide range of compositions of about 11 at% in which the transition zone occurs. However, even when working in the transition zone, the film appears to be completely amorphous for thicknesses in the region marked with green dotted lines and is completely amorphous below h_c (Figure 4e). Similarly, looking from the surface, the film seems to be completely nanocrystalline for thicknesses in the region marked with orange dotted lines. This thickness-composition phase diagram sends an important message: due to composition-dependent kinetics and critical nucleation thickness, the peculiar bi-phased topography can easily be missed experimentally, explaining why details of such transition have not been considered and possibility of functional properties manipulation has been missed.

4. Conclusions

In conclusion, we developed a novel and simple bottom-up route, extendable to a wide range of alloys, for the design of multifunctional surfaces. By working in the amorphous-to-crystalline structural transition in thin films, competitive growth between crystalline and amorphous phases may occurs. The resulting surface morphology can be controlled by thickness and composition, consequently, surface-related properties such as optical reflectance and wettability are manipulated to a large extent. Further, we developed a model capable of describing the kinetics of the nanocrystalline-amorphous competitive growth. As original aspects, the model adapts the MKM approach used for 2D phase transformation to successfully describe the kinetics of competitive growth in thin films. Finally, a phase

diagram is proposed showing that, despite the existence of a wide range of compositions for the nanocrystalline-amorphous competitive growth, the dependency of nucleation and growth to the film thickness can easily hide the phenomenon in experiments. These results provide a platform to track down and control the process in other alloys and for the design of functionally graded surfaces.

5. Appendices

Appendix A: Kinetics of nanocrystalline-amorphous competitive growth

We start assuming an Avrami nucleation mechanism, meaning in our case that the nucleation of the nanocrystalline phase occurs at certain sites in the sample, which are gradually exhausted upon film growth [53–55]. Let N be the number of particles of the nanocrystalline phase (growth nuclei) per unit area and N_{germ} the number of germ nuclei per unit area from which the growth nuclei are formed, such that the total number of growth and germ nuclei per unit area N_0 is constant. Thus, the change in the density of growth nuclei can be written as $dN/dt = -dN_{germ}/dt = \lambda\, N_{germ}$ [38–41], where λ is the rate at which an individual germ nucleus becomes in a growth nucleus. After integration, considering the boundary condition that the density of germ nuclei equals N_0 at $t = 0$, the density of growth nuclei is given by

$$N_{(t)} = N_0 \left(1 - e^{-\int_0^t \lambda\, dt}\right). \quad \text{(A.1)}$$

The nature of the apparent 2D phase transformation presented here makes possible the use of film thickness h as a replacement of time t as the variable that controls the grade of transformation. Considering that the deposition rate of the film V_0 is constant, the sample thickness is $h = V_0\, t$ and, in this way, all the expressions obtained can be expressed as a function of film thickness. Thus, the density of growth nuclei can be re-written as:

$$N_{(h)} = N_0 \left(1 - e^{-\frac{1}{V_0}\int_0^h \lambda\, dh}\right) \quad \text{(A.2)}$$

and its derivative (the nucleation rate) as:

$$\frac{dN}{dh} = \frac{\lambda}{V_0} N_0 e^{-\frac{1}{V_0}\int_0^h \lambda\, dh} \tag{A.3}$$

An important point in our approach is how to express the rate λ. It is usually supposed that λ obeys Arrhenius-type temperature dependence: $\lambda = \lambda_0 e^{-\frac{Q_n}{RT}}$, where λ_0 is a temperature-independent rate and Q_N is the activation energy (energy barrier) for nucleation [38–41,53]. In our case, the experimental evidence is pointing to the conclusion that there is a thickness from which nucleation starts, i.e., there is an incubation thickness. This indicates that the activation energy for the nucleation of the crystalline phase $Q_N \gg RT$ at the beginning of the film growth. Consequently, the films starts to grow amorphous. With the increase of the film thickness, the crystalline phase starts to nucleate, which implies that the energy barrier Q_N becomes of the order of RT. The reasons behind this modification could be thermal, chemical (a local change in composition due to the preferred segregation of one of the species to the grain boundaries, which favors the nucleation [32]), mechanical (local changes of the strain energy due to the heterogeneous distributions of the film stress [56,57] which can decrease the energy barrier), among others. Considering this, we propose to write λ as follows:

$$\lambda = \lambda_0 e^{-\frac{Q_n}{RT}} \Theta[h - h_c], \tag{A.4}$$

where Θ is the unitary-step Heaviside function and h_c is the critical thickness from which nucleation starts. Equation A.4 is a simplification of the real scenario presented above where a gradual evolution of $\frac{Q_N}{RT}$ occurs instead of the sudden change of Θ. Nevertheless, the use of Θ simplifies all the derived equations, yet retaining the physics of the phenomenon. Thereby, Equation A.2 and A.3 follow the dependencies:

$$N_{(h)} = N_0\left(1 - e^{-\gamma(h-h_c)}\right)\Theta[h - h_c] \tag{A.5}$$

and

$$\frac{dN}{dh} = \gamma N_0 e^{-\gamma(h-h_c)}\Theta[h-h_c] \quad \text{(A.6)}$$

where $\gamma = \frac{\lambda_0}{V_0} e^{-\frac{Q_n}{RT}}$. In this way, through Equation A.5, the evolution of the density of growth nuclei with thickness can be calculated.

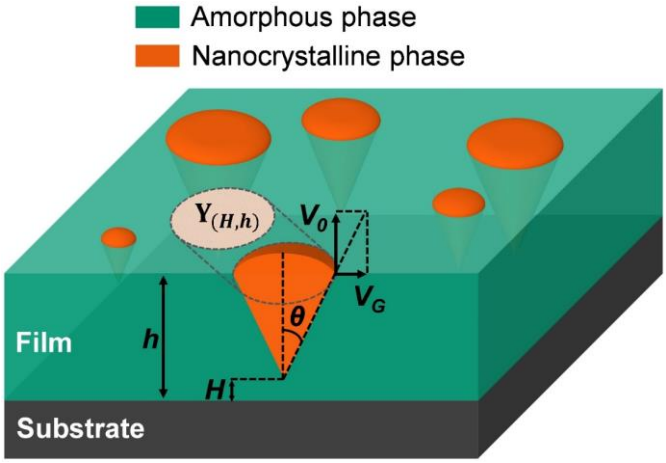

Figure A.1. Schematic of film presenting nanocrystalline-amorphous competitive growth. Some key parameters are shown: h (thickness of the film), H (thickness at which a determined nanocrystalline region nucleates), θ (angle between the generatrix and the axis of the cone of nanocrystalline region), V_G (growth velocity of the nanocrystalline phase in the in-plane direction), V_0 (deposition rate of the film), $Y_{(H,h)}$ (projected area at a film thickness h of a nucleus nucleated at a film thickness H).

The so-called "extended transformed fraction" is defined as $\chi_e = \frac{S_e}{S}$, where S_e represents the projected area, perpendicular to the growth direction, of nanocrystalline regions if they could each nucleate and grow in the absence of other interfering growing nuclei. S is the total surface area. The evolution of χ_e with time, derived in the framework of the MKM approach [38–41], can be re-written as a function of h:

$$\chi_e(h) = \int_0^h \left(\frac{dN}{dh}\right)_{(H)} Y_{(H,h)} dH \quad \text{(A.7)}$$

where $\frac{dN}{dh}$ is given by Equation A.6 and $Y_{(H,h)}$ represents the projected area at a film thickness h of a nucleus nucleated at a film thickness H (see Figure A.1). Thus, $Y_{(H,h)}$ can be written as:

$$Y_{(H,h)} = \pi \left(\frac{V_G}{V_0}\right)^2 (h - H)^2 \tag{A.8}$$

where V_G is the growth velocity of the nanocrystalline phase in the in-plane direction (see Figure A.1). Using Equation A.6 and A.8 the extended transformed fraction is obtained:

$$\chi_e(h) = \pi N_0 \left(\frac{V_G}{V_0}\right)^2 \gamma e^{\gamma h_c} I \Theta[h - h_c] \tag{A.9}$$

where $I = \int_{h_c}^{h} (h - H)^2 e^{-\gamma H} dH$. After integration of I, the final expression for the extended transformed fraction is given by

$$\chi_e(h) = \pi \left(\frac{V_G}{V_0}\right)^2 \frac{N_0}{\gamma^2} \Upsilon \Theta[h - h_c] \tag{A.10}$$

where $\Upsilon = -2e^{-\gamma(h-h_c)} + (\gamma(h - h_c) - 1)^2 + 1$.

Equation A.10 has as free parameters the three of Equation A.5: N_0, γ and h_c, and the ratio $\frac{V_G}{V_0}$ between the in-plane growth velocity and the deposition rate. From the schematic shown in Figure A.1 follows that $\frac{V_G}{V_0} = \tan(\theta)$, where θ is the angle between the generatrix and the axis of the cone of nanocrystalline zone. The analysis of several cross-section images reveals that θ can be considered constant for all the samples studied and can be approximated to $\theta = 22°$. Thus $\frac{V_G}{V_0} = 0.404$ can be fixed and Equation A.5 and A.10 have both the same free parameters.

The relation between the extended transformed fraction and the surface coverage by the nanocrystalline phase (real transformed fraction) S depends on the spatial distribution of the nanocrystalline nuclei in the amorphous phase. If a random nucleation (RN) of the

nanocrystalline phase is supposed, $S = 1 - e^{-\chi_e}$ which corresponds to the case of the classical KJMA approach [53–55,51,52]. However, if nuclei are not randomly distributed, for example, when grain boundaries nucleation (GBN) occurs, this relation is not fulfilled. A phenomenological approach accounting for impingement in this case is often used and S can be written as a function of χ_e as follows:

$$S_{(h)} = 1 - \left(1 + (\xi - 1)\chi_{e_{(h)}}\right)^{-1/\xi - 1} \quad \text{(A.11)}$$

where ξ is the so-called "impingement parameter" [41]. Thus, for $\xi > 1$ impingement is stronger than in the case of RN and when $\xi \to 1$, RN model is recovered.

In summary, Equation A.5 can be fitted to the data of density of nanocrystalline nuclei, using N_0, γ and h_c as free parameters. The parameters obtained from the fitting can be evaluated in Equation A.10. In this way, the evolution of the extended transformed fraction χ_e with the sample thickness can be calculated. Then, Equation A.11 can be fitted to the surface coverage using ξ as free parameter.

Appendix B: Determining the range of composition of the transition zone

As we pointed-out, biphased films are obtained in the transition zone and the proportion between the nanocrystalline and the amorphous phase can be controlled either by varying the composition or the thickness of the films. In the Zr-W system, this occurs when the W content is varied in the range $W_a < W < W_c$. Films are single-phased amorphous for $W \leq W_a$ and single-phased nanocrystalline for $W \geq W_c$. W_a and W_c can be determined by using the evolution of the density of nucleation sites N_0 with composition (Figure 4c) and considering that N_0 satisfies the boundary conditions: $N_0 = 0$ when $W = W_a$ and $N_0 \to \infty$ when $W = W_c$. Note that, at the same time $h_c = 0$ when $W = W_c$ as follows from the definition of W_c.

Thereby, the following empirical dependency between N_0 and W, which satisfies the boundary conditions, can be assumed:

$$N_0 = A\left(\frac{W-W_a}{W_c-W}\right) \quad \text{(B.1)}$$

where A is a constant. From Equation B.1, $W_a = 65.9$ at% and $W_c = 77.4$ at% are calculated. Note that the transition zone occurs in a range of compositions of about $\Delta W = W_c - W_a \approx 11$ at%.

Declaration of Competing Interest

The authors declare that they have no known competing financial interests or personal relationships that could have appeared to influence the work reported in this paper.

Acknowledgements

The "Université franco-allemande" (UFA) and the "Ministère de l'Enseignement Supérieur et de la Recherche" are deeply acknowledged for the PhD scholarship of Alejandro Borroto within the PhD-track in Materials Science and Engineering at UFA. The Daυm competence center of IJL is deeply acknowledged for access to UHV magnetron sputtering deposition facility.

References

[1] C. Neinhuis, Characterization and Distribution of Water-repellent, Self-cleaning Plant Surfaces, Annals of Botany. 79 (1997) 667–677. https://doi.org/10.1006/anbo.1997.0400.
[2] K. Autumn, Y.A. Liang, S.T. Hsieh, W. Zesch, W.P. Chan, T.W. Kenny, R. Fearing, R.J. Full, Adhesive force of a single gecko foot-hair, Nature. 405 (2000) 681–685. https://doi.org/10.1038/35015073.
[3] P.B. Clapham, M.C. Hutley, Reduction of Lens Reflexion by the "Moth Eye" Principle, Nature. 244 (1973) 281–282. https://doi.org/10.1038/244281a0.
[4] P. Vukusic, J.R. Sambles, Photonic structures in biology, Nature. 424 (2003) 852–855. https://doi.org/10.1038/nature01941.
[5] B. Dean, B. Bhushan, Shark-skin surfaces for fluid-drag reduction in turbulent flow: a review, Philosophical Transactions of the Royal Society A: Mathematical, Physical and Engineering Sciences. 368 (2010) 4775–4806. https://doi.org/10.1098/rsta.2010.0201.

[6] L. Feng, S. Li, Y. Li, H. Li, L. Zhang, J. Zhai, Y. Song, B. Liu, L. Jiang, D. Zhu, Super-Hydrophobic Surfaces: From Natural to Artificial, Advanced Materials. 14 (2002) 1857–1860. https://doi.org/10.1002/adma.200290020.
[7] R. Blossey, Self-cleaning surfaces — virtual realities, Nature Materials. 2 (2003) 301–306. https://doi.org/10.1038/nmat856.
[8] H. Lee, B.P. Lee, P.B. Messersmith, A reversible wet/dry adhesive inspired by mussels and geckos, Nature. 448 (2007) 338–341. https://doi.org/10.1038/nature05968.
[9] Y.-F. Huang, S. Chattopadhyay, Y.-J. Jen, C.-Y. Peng, T.-A. Liu, Y.-K. Hsu, C.-L. Pan, H.-C. Lo, C.-H. Hsu, Y.-H. Chang, C.-S. Lee, K.-H. Chen, L.-C. Chen, Improved broadband and quasi-omnidirectional anti-reflection properties with biomimetic silicon nanostructures, Nature Nanotechnology. 2 (2007) 770–774. https://doi.org/10.1038/nnano.2007.389.
[10] W.-L. Min, B. Jiang, P. Jiang, Bioinspired Self-Cleaning Antireflection Coatings, Advanced Materials. 20 (2008) 3914–3918. https://doi.org/10.1002/adma.200800791.
[11] K.-C. Hsieh, T.-Y. Tsai, D. Wan, H.-L. Chen, N.-H. Tai, Iridescence of Patterned Carbon Nanotube Forests on Flexible Substrates: From Darkest Materials to Colorful Films, ACS Nano. 4 (2010) 1327–1336. https://doi.org/10.1021/nn901910h.
[12] G.D. Bixler, B. Bhushan, Fluid Drag Reduction with Shark-Skin Riblet Inspired Microstructured Surfaces, Advanced Functional Materials. 23 (2013) 4507–4528. https://doi.org/10.1002/adfm.201203683.
[13] S. Calderon Velasco, A. Cavaleiro, S. Carvalho, Functional properties of ceramic-Ag nanocomposite coatings produced by magnetron sputtering, Progress in Materials Science. 84 (2016) 158–191. https://doi.org/10.1016/j.pmatsci.2016.09.005.
[14] C. de Melo, M. Jullien, Y. Battie, A. En Naciri, J. Ghanbaja, F. Montaigne, J.-F. Pierson, F. Rigoni, N. Almqvist, A. Vomiero, S. Migot, F. Mücklich, D. Horwat, Semi-Transparent p-Cu2O/n-ZnO Nanoscale-Film Heterojunctions for Photodetection and Photovoltaic Applications, ACS Appl. Nano Mater. 2 (2019) 4358–4366. https://doi.org/10.1021/acsanm.9b00808.
[15] A. Chen, Z. Harrell, P. Lu, E. Enriquez, L. Li, B. Zhang, P. Dowden, C. Chen, H. Wang, J.L. MacManus-Driscoll, Q. Jia, Strain Enhanced Functionality in a Bottom-Up Approach Enabled 3D Super-Nanocomposites, Advanced Functional Materials. 29 (2019) 1900442. https://doi.org/10.1002/adfm.201900442.
[16] B.A. Movchan, A.V. Demchishin, Structure and properties of thick condensates of nickel, titanium, tungsten, aluminum oxides, and zirconium dioxide in vacuum, Fiz. Metal. Metalloved. 28 (1969) 653.
[17] J.A. Thornton, Influence of apparatus geometry and deposition conditions on the structure and topography of thick sputtered coatings, Journal of Vacuum Science and Technology. 11 (1974) 666–670. https://doi.org/10.1116/1.1312732.
[18] A. Anders, A structure zone diagram including plasma-based deposition and ion etching, Thin Solid Films. 518 (2010) 4087–4090. https://doi.org/10.1016/j.tsf.2009.10.145.
[19] Y. Li, Q. Guo, J.A. Kalb, C.V. Thompson, Matching Glass-Forming Ability with the Density of the Amorphous Phase, Science. 322 (2008) 1816–1819. https://doi.org/10.1126/science.1163062.
[20] J.P. Chu, J.S.C. Jang, J.C. Huang, H.S. Chou, Y. Yang, J.C. Ye, Y.C. Wang, J.W. Lee, F.X. Liu, P.K. Liaw, Y.C. Chen, C.M. Lee, C.L. Li, C. Rullyani, Thin film metallic glasses: Unique properties and potential applications, Thin Solid Films. 520 (2012) 5097–5122. https://doi.org/10.1016/j.tsf.2012.03.092.
[21] H.-B. Yu, Y. Luo, K. Samwer, Ultrastable Metallic Glass, Advanced Materials. 25 (2013) 5904–5908. https://doi.org/10.1002/adma.201302700.

[22] Y. Liu, J. Liu, S. Sohn, Y. Li, J.J. Cha, J. Schroers, Metallic glass nanostructures of tunable shape and composition, Nature Communications. 6 (2015). https://doi.org/10.1038/ncomms8043.
[23] W. Diyatmika, J.P. Chu, B.T. Kacha, C.-C. Yu, C.-M. Lee, Thin film metallic glasses in optoelectronic, magnetic, and electronic applications: A recent update, Current Opinion in Solid State and Materials Science. 19 (2015) 95–106. https://doi.org/10.1016/j.cossms.2015.01.001.
[24] B.R. Braeckman, D. Depla, On the amorphous nature of sputtered thin film alloys, Acta Materialia. 109 (2016) 323–329. https://doi.org/10.1016/j.actamat.2016.02.035.
[25] S. Das, H.S. Arora, S. Mukherjee, Metallic Glass Nano-composite Thin Films for High-performance Functional Applications, JOM. 69 (2017) 1165–1169. https://doi.org/10.1007/s11837-017-2365-z.
[26] C.-C. Yu, C.M. Lee, J.P. Chu, J.E. Greene, P.K. Liaw, Fracture-resistant thin-film metallic glass: Ultra-high plasticity at room temperature, APL Materials. 4 (2016) 116101. https://doi.org/10.1063/1.4966932.
[27] Y. Liu, J. Padmanabhan, B. Cheung, J. Liu, Z. Chen, B.E. Scanley, D. Wesolowski, M. Pressley, C.C. Broadbridge, S. Altman, U.D. Schwarz, T.R. Kyriakides, J. Schroers, Combinatorial development of antibacterial Zr-Cu-Al-Ag thin film metallic glasses, Scientific Reports. 6 (2016). https://doi.org/10.1038/srep26950.
[28] A. Etiemble, C. Der Loughian, M. Apreutesei, C. Langlois, S. Cardinal, J.M. Pelletier, J.-F. Pierson, P. Steyer, Innovative Zr-Cu-Ag thin film metallic glass deposed by magnetron PVD sputtering for antibacterial applications, Journal of Alloys and Compounds. 707 (2017) 155–161. https://doi.org/10.1016/j.jallcom.2016.12.259.
[29] M.M. Khan, I. Shabib, W. Haider, A combinatorially developed Zr-Ti-Fe-Al metallic glass with outstanding corrosion resistance for implantable medical devices, Scripta Materialia. 162 (2019) 223–229. https://doi.org/10.1016/j.scriptamat.2018.11.011.
[30] D. Horwat, E. Jimenez-Pique, J.F. Pierson, S. Migot, M. Dehmas, M. Anglada, High hardness, low Young's modulus and low friction of nanocrystalline ZrW_2 Laves phase and $Zr_{1-x}W_x$ thin films, Journal of Physics and Chemistry of Solids. 73 (2012) 554–558. https://doi.org/10.1016/j.jpcs.2011.12.009.
[31] A. Borroto, S. Bruyère, N. Thurieau, C. Gendarme, E. Jimenez-Piqué, J.J. Roa, J.F. Pierson, F. Mücklich, D. Horwat, Structural and mechanical properties of $Zr_{1-x}Mo_x$ thin films: From the nano-crystalline to the amorphous state, Journal of Alloys and Compounds. 729 (2017) 137–143. https://doi.org/10.1016/j.jallcom.2017.09.153.
[32] A. Borroto, S. Bruyère, S. Migot, J.F. Pierson, T. Gries, F. Mücklich, D. Horwat, Controlling surface morphology by nanocrystalline/amorphous competitive self-phase separation in thin films: Thickness-modulated reflectance and interference phenomena, Acta Materialia. 181 (2019) 78–86. https://doi.org/10.1016/j.actamat.2019.09.036.
[33] Z.Z. Tang, J.H. Hsieh, S.Y. Zhang, C. Li, Y.Q. Fu, Phase transition and microstructure change in Ta–Zr alloy films by co-sputtering, Surface and Coatings Technology. 198 (2005) 110–113. https://doi.org/10.1016/j.surfcoat.2004.10.019.
[34] P. Sharma, H. Kimura, A. Inoue, Magnetic behavior of cosputtered Fe-Zr amorphous thin films exhibiting perpendicular magnetic anisotropy, Physical Review B. 78 (2008) 134414. https://doi.org/10.1103/PhysRevB.78.134414.
[35] D. Horwat, M. Dehmas, E. Aubry, J. Zollinger, S. Migot, J.F. Pierson, Properties of nanocrystalline and nanocomposite W_xZr_{1-x} thin films deposited by co-sputtering, Intermetallics. 17 (2009) 421–426. https://doi.org/10.1016/j.intermet.2008.11.020.
[36] D.J.M. King, S.C. Middleburgh, A.C.Y. Liu, H.A. Tahini, G.R. Lumpkin, M.B. Cortie, Formation and structure of V–Zr amorphous alloy thin films, Acta Materialia. 83 (2015) 269–275. https://doi.org/10.1016/j.actamat.2014.10.016.

[37] M. Apreutesei, P. Steyer, A. Billard, L. Joly-Pottuz, C. Esnouf, Zr–Cu thin film metallic glasses: An assessment of the thermal stability and phases' transformation mechanisms, Journal of Alloys and Compounds. 619 (2015) 284–292. https://doi.org/10.1016/j.jallcom.2014.08.253.
[38] A.T.W. Kempen, F. Sommer, E.J. Mittemeijer, Determination and interpretation of isothermal and non-isothermal transformation kinetics; the effective activation energies in terms of nucleation and growth, Journal of Materials Science. 37 (2002) 1321–1332. https://doi.org/10.1023/A:1014556109351.
[39] E.J. Mittemeijer, F. Sommer, Solid state phase transformation kinetics: a modular transformation model, Zeitschrift Für Metallkunde. 93 (2002) 352–361. https://doi.org/10.3139/146.020352.
[40] F. Liu, F. Sommer, C. Bos, E.J. Mittemeijer, Analysis of solid state phase transformation kinetics: models and recipes, International Materials Reviews. 52 (2007) 193–212. https://doi.org/10.1179/174328007X160308.
[41] E.A. Jägle, E.J. Mittemeijer, The kinetics of grain-boundary nucleated phase transformations: Simulations and modelling, Acta Materialia. 59 (2011) 5775–5786. https://doi.org/10.1016/j.actamat.2011.05.054.
[42] J. Bhattarai, E. Akiyama, H. Habazaki, A. Kawashima, K. Asami, K. Hashimoto, Electrochemical and xps studies of the corrosion behavior of sputter-deposited amorphous W-Zr alloys in 6 and 12 M HCl solutions, Corrosion Science. 39 (1997) 355–375. https://doi.org/10.1016/S0010-938X(97)83351-3.
[43] R. Jerlerud Pérez, B. Sundman, Thermodynamic assessment of the Mo–Zr binary phase diagram, Calphad. 27 (2003) 253–262. https://doi.org/10.1016/j.calphad.2003.09.003.
[44] P. Zhou, Y. Peng, Y. Du, S. Wang, G. Wen, Thermodynamic modeling of the C–W–Zr system, International Journal of Refractory Metals and Hard Materials. 50 (2015) 274–281. https://doi.org/10.1016/j.ijrmhm.2015.02.002.
[45] J.M. López, J.A. Alonso, L.J. Gallego, Determination of the glass-forming concentration range in binary alloys from a semiempirical theory: Application to Zr-based alloys, Physical Review B. 36 (1987) 3716–3722. https://doi.org/10.1103/PhysRevB.36.3716.
[46] S. Zhao, J.H. Li, S.M. An, S.N. Li, B.X. Liu, Atomistic modeling to investigate the favored composition for metallic glass formation in the Ca–Mg–Ni ternary system, Physical Chemistry Chemical Physics. 19 (2017) 12056–12063. https://doi.org/10.1039/C7CP00466D.
[47] R. Raj, R. Enright, Y. Zhu, S. Adera, E.N. Wang, Unified Model for Contact Angle Hysteresis on Heterogeneous and Superhydrophobic Surfaces, Langmuir. 28 (2012) 15777–15788. https://doi.org/10.1021/la303070s.
[48] J.S. Ahn, T.R. Hendricks, I. Lee, Control of Specular and Diffuse Reflection of Light Using Particle Self-Assembly at the Polymer and Metal Interface, Advanced Functional Materials. 17 (2007) 3619–3625. https://doi.org/10.1002/adfm.200700251.
[49] V. Brien, P. Miska, B. Bolle, P. Pigeat, Columnar growth of ALN by r.f. magnetron sputtering: Role of the {$101\bar{3}$} planes, Journal of Crystal Growth. 307 (2007) 245–252. https://doi.org/10.1016/j.jcrysgro.2007.06.013.
[50] R. Gago, M. Vinnichenko, A. Redondo-Cubero, Z. Czigány, L. Vázquez, Surface Morphology of Heterogeneous Nanocrystalline Rutile/Amorphous Anatase TiO_2 Films Grown by Reactive Pulsed Magnetron Sputtering, Plasma Processes Polym. 7 (2010) 813–823. https://doi.org/10.1002/ppap.200900182.
[51] A.N. Kolmogorov, On the statistical theory of the crystallization of metals, Bull. Acad. Sci. USSR, Math. Ser. 3 (1937) 355.
[52] W.A. Johnson, R.F. Mehl, Reaction kinetics in processes of nucleation and growth, Trans. Am. Inst. Min. Eng. 135 (1939) 416.

[53] M. Avrami, Kinetics of Phase Change. I General Theory, The Journal of Chemical Physics. 7 (1939) 1103–1112. https://doi.org/10.1063/1.1750380.
[54] M. Avrami, Kinetics of Phase Change. II Transformation-Time Relations for Random Distribution of Nuclei, The Journal of Chemical Physics. 8 (1940) 212–224. https://doi.org/10.1063/1.1750631.
[55] M. Avrami, Granulation, Phase Change, and Microstructure Kinetics of Phase Change. III, The Journal of Chemical Physics. 9 (1941) 177–184. https://doi.org/10.1063/1.1750872.
[56] E. Vasco, C. Polop, Intrinsic Compressive Stress in Polycrystalline Films is Localized at Edges of the Grain Boundaries, Physical Review Letters. 119 (2017) 256102. https://doi.org/10.1103/PhysRevLett.119.256102.
[57] E. Vasco, E.G. Michel, C. Polop, Disclosing the origin of the postcoalescence compressive stress in polycrystalline films by nanoscale stress mapping, Physical Review B. 98 (2018) 195428. https://doi.org/10.1103/PhysRevB.98.195428.